

Multipolar Ferrite Assisted Synchronous Reluctance machines: a general design approach

Original

Multipolar Ferrite Assisted Synchronous Reluctance machines: a general design approach / Boazzo, Barbara; Vagati, Alfredo; Pellegrino, GIAN - MARIO LUIGI; Armando, Eric Giacomo; Guglielmi, Paolo. - In: IEEE TRANSACTIONS ON INDUSTRIAL ELECTRONICS. - ISSN 0278-0046. - STAMPA. - 62:2(2014), pp. 832-845. [10.1109/TIE.2014.2349880]

Availability:

This version is available at: 11583/2573561 since:

Publisher:

IEEE - INST ELECTRICAL ELECTRONICS ENGINEERS INC

Published

DOI:10.1109/TIE.2014.2349880

Terms of use:

This article is made available under terms and conditions as specified in the corresponding bibliographic description in the repository

Publisher copyright

(Article begins on next page)

Multipolar Ferrite Assisted Synchronous Reluctance machines: a general design approach

Abstract—The design of multipolar Ferrite Assisted Synchronous Reluctance (FASR) machines is formalized via a two steps procedure. At first one rectified machine pole is analyzed and key figures of merit are expressed in equations and discussed to derive general guidelines for high performance designs. Then, multipolar rotating machines are modeled as the combination of multiple rectified poles within a stack cylinder having constrained outer dimensions. It is demonstrated that, at given output torque, the number of poles can be optimized either to minimize the Joule loss or to minimize the remanence of the ferrite magnets. The design approach is both FEA and experimentally tested on a prototype FASR machine, rated about 800 Nm at 168 rpm. The prototype has been designed for direct drive lift applications, showing similar performances, if fairly compared to the ones of previous solutions based on rare-earth magnets.

Index Terms— Hard ferrite magnets, Synchronous motor drives, Demagnetization, Direct drive applications, Wind turbine generators.

I. INTRODUCTION

Permanent Magnet (PM) machines have been the most performing electric actuators, in terms of torque density and efficiency, since the adoption of rare-earth magnets, which offer large energy products and ideal recoil characteristics over wide ranges of temperatures. However, the recent price volatility of rare earth raw materials has been compelling designers and manufacturers of electric motors to test alternative solutions, using no PMs [1]-[2], a reduced amount of rare-earth PMs [3]-[4], or lower energy density PMs, such as hard ferrites [5]-[12].

The mere substitution of high energy magnets with ferrite ones into standard Surface-mounted PM (SPM) and Interior PM (IPM) rotor configurations cannot lead to satisfactory designs [6]-[7], since both SPM and IPM motors mainly rely on Nd- or Sm-based materials for their high performance [13]-[14]. A more effective way [8]-[10] to exploit lower energy density magnets is to PM-assist Synchronous Reluctance (SR) machines, having multi-layer rotor structures (i.e. valuable starting designs in terms of torque density). In this case, the magnet excitation is needed only as an additional contribute to the torque and an improvement for the Power Factor (PF) and the speed range of the drive. As a result, FASR machines can

compete with rare-earth based SPM and IPM counterparts, despite the lower energy density of ferrite materials [8], [9].

Ferrites are also known to be prone to demagnetization at low temperatures. Recent papers have put in evidence that, when dealing with low temperature environments, the flux barriers of FASR rotor types must be shaped properly [11]-[12] and a pre-heating or a temporary derating of the machine output torque might be necessary [12].

This paper sums up the geometric rules needed for optimizing the starting SR design and increasing the robustness against demagnetization of FASR motors. It gives also fully analytical expressions for the design and evaluation of such these machines. In the first sections, reference is made to one rectified pole, as the one in Fig. 1, with the flux barriers having constant thickness along their widths and being completely filled with ferrites, so to compensate for their low B-H energy products. Figures of merit such as shear stress, Joule loss density and power factor are expressed in equations, as functions of per-unit (pu) quantities, and the maximum current loading according to irreversible demagnetization is quantified. Afterwards, the elementary blocks are assembled to form a rotating machine fitting into fixed stack dimensions (stator diameter and stack length). The design space is identified according to the results of the pu analysis on the reference block and straightforward equations are proposed to choose the pole pairs number of the machine in order to minimize either the Joule loss or the PM grade, at given torque. The proposed design procedure is both FEA and experimentally validated.

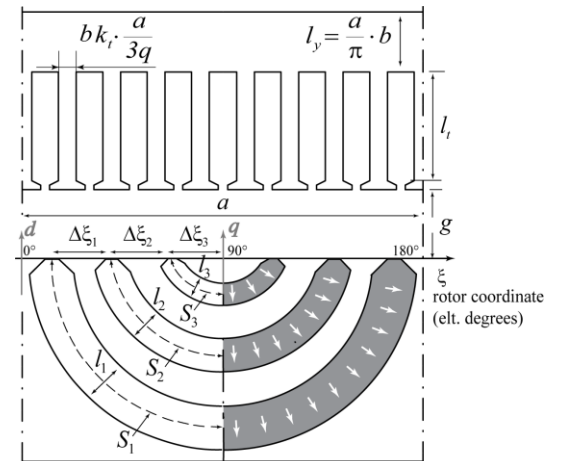


Fig. 1. Rectified pole of a FASR machine with a three-layer rotor and the PMs magnetized radial-wise. The dq axes follow the SR model approach.

II. GENERAL ASSUMPTIONS AND ROTOR MODEL

A. Reference geometry

The key-geometric parameters in Fig. 1 are: the airgap length (g), the pole pitch (a), the stator tooth length (l_t), the pitch of the k -th rotor “slot” ($\Delta\xi_k$), half the width of the k -th layer (S_k) and its uniform thickness (l_k). The parameters b and k_t will be introduced in Subsection III.A; q is the slot number per pole per phase; l is the stack length of the reference block.

As for the number of rotor flux barriers (n) and their shapes, different choices are possible. Round barriers are sketched in Fig. 1 only for simplicity. In fact, actual rotor designs are typically optimized to improve the saliency ratio between the d- and q-axis. Since a PM-assisted SR machine is analyzed here, the dq axes follow the SR model approach (that is, the d-axis is aligned to the maximum permeance direction).

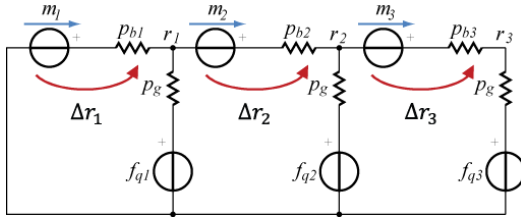


Fig. 2. The equivalent circuit represents the q-axis magnetic behavior of half a pole. It refers to the FASR example rotor in Fig. 1 ($n=3$).

B. q-axis magnetic model

The circuit in Fig. 2 shows the q-axis magnetic model of the 3-barrier rotor reported in Fig.1. This represents a simplified version, as structural ribs are not taken into account yet. The fluxes are the ones of half a pole. The magneto-motive force (mmf) generators, magnetic potentials and permeances are expressed in normalized quantities according to the base values listed in Table I.

TABLE I
NORMALIZATION OF THE Q-AXIS MAGNETIC MODEL

Quantity	Base value
Magneto-motive forces, magnetic potentials	Peak F_q of the fundamental q-axis stator mmf waveform
Permeances	$\mu_0 l$
Fluxes	$F_q \mu_0 l$

The m_{123} generators and the respective barrier permeances p_{b123} model the layers filled with ferrite magnets. The terms p_g are the permeances of the rotor teeth at the airgap. The mmf generators f_{q123} stand for the effect of the q-axis stator current, oriented against the PMs. The fundamental wave of the stator mmf, in pu of its peak value F_q , is averaged across each rotor tooth at the airgap and then modeled via the staircase f_{q123} reported in Fig. 3 [12], [15]. The model accounts for the polarization of the rotor flux guides into the potentials r_{123} , assumed to be uniform along the guides width.

If the rotor geometry is designed for having both the PMs mmf m_{123} and the magnetic potential drops Δr_{123} proportional to the stator mmf staircase, as in Fig. 3, the harmonic content of the quadrature flux density is minimized and all the PMs work at the same flux density, at all current level. The main geometric rules leading to this twofold purpose are discussed in the next section, even if more details can be found in [12].

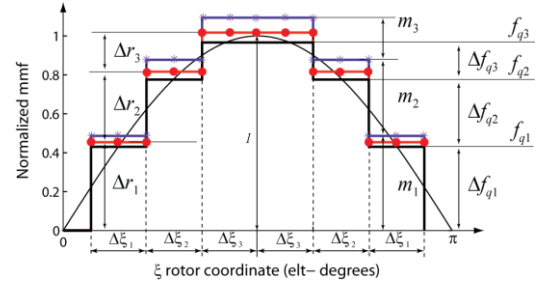


Fig. 3. Staircase distributions of the mmfs of Fig. 2, in pu of the peak value of the q-axis fundamental mmf. No markers: q-axis stator mmf f_{q123} . Star: PMs mmf m_{123} . Circle: iron guides magnetic potentials r_{123} .

C. Main geometric constraints for the rotor design

The rotor geometry is based on four design criteria:

1. the rotor pitch is “regular”;
2. the barriers have constant thickness throughout their respective spans;
3. the barriers thicknesses l_{123} follow the proportion of the pu steps Δf_{q123} , that model the q-axis stator mmf;
4. also the barriers widths S_{123} follow the proportions defined in point 3.

The first condition refers to torque ripple minimization via proper displacement of the flux barriers at the airgap [2], [16]. The equivalent number of rotor slots per pole pair n_r is introduced and the “regular” inter-barrier pitch $\Delta\xi$ is defined:

$$\Delta\xi = \frac{2\pi}{n_r} \quad (1)$$

Different choices of n_r are possible, in order to avoid the direct interaction between stator and rotor slot harmonics [17]. If $n_r=4n+2$, the rotor “slot” pitch $\Delta\xi_k$ is kept constant, and equal to $\Delta\xi$, along the whole periphery of the rotor. If $n_r>4n+2$, the inter-barrier pitch can be still uniform, with the general exception of the angle $\Delta\xi_n$ (between the smallest layer and the q-axis) that is larger than $\Delta\xi$. The most “regular” rotor topologies are called “complete” in [17] and they are the ones, this paper refers to, for simplicity. To deal with “non-complete” machines, the following equations need little modifications and one extra parameter (that is, $\Delta\xi_n$).

The second constraint in the list comes from the idea that, in case some parts of the barriers (i.e. of the magnets) would be thinner, there the flux density would be lower and thus closer to irreversible demagnetization.

With all the flux barriers having constant thicknesses, the mmf m_{123} follow directly from l_{123} [12]. Thus, in order to make the PMs mmf staircase proportional to the stator one, the third geometrical constraint is required. In formula:

$$l_k = l_a \cdot \frac{\Delta f_{qk}}{f_{qn}} \quad k = 1, 2, \dots, n \quad (2)$$

l_a is the total insulation, sum of l_{123} . f_{qn} is the top value of the pu n -steps staircase, that reproduces the stator mmf along the q-axis. f_{qn} is always close to one, whatever the number of layers is (for example $f_{q3} = 0.967$ when $n=3$ and $n_r=14$, as in the “complete” reference rotor of Fig. 1).

Once the magnet thicknesses l_{123} and then the mmf m_{123} are set as suggested by (2), the magnetic potentials r_{123} are proportional to the pu steps f_{q123} , if all the layers have the same

permeance [12]. At this purpose, the fourth condition (3) about the barrier widths S_{123} is needed.

$$S_k = S_1 \frac{l_k}{l_1} \quad k = 1, 2, \dots, n \quad (3)$$

III. KEY DESIGN EQUATION

This section provides pu expressions for the design of both the magnetic and electric loading of the reference block in Fig. 1. The magnetic loading B_{gap} [T] is defined here as the peak flux density in the airgap. The electric loading A [Apk/m] is proportional to the fundamental peak value F of the stator mmf waveform:

$$A = \frac{\pi}{2} \cdot \frac{F}{a} = \frac{\pi}{2} \cdot \frac{1}{a} \cdot \left(\frac{3}{\pi} k_w N I \right) \quad (4)$$

I is the peak value of the stator current, N is the number of conductors in series per pole per phase and k_w is the winding factor.

A. d-axis magnetizing loading

A portion of the total electric loading has to be spent for generating the d-axis magnetizing loading $B_{gap,d}$, which is typically required to be around 0.75-0.9 T.

The value of $B_{gap,d}$ is strictly related to the size of the stator back iron and its exploitation in terms of flux density. In fact, if the q-axis flux is nearly zeroed by the PMs action, as it is the case with effective PM-assisted designs, the stator yoke and teeth are interested mainly by the d-axis flux. Then, the chosen magnetizing loading in the airgap ($B_{gap,d}$) and the target flux density in the back iron (B_{fe}) determine the core dimension. As highlighted in Fig. 1, the ratio b between $B_{gap,d}$ and B_{fe} represents: the yoke height, in pu of the pole pitch, and the tooth width, in pu of the slot pitch, being k_t a scaling factor slightly lower than one. b is usually between 0.5 and 0.65.

Once $B_{gap,d}$ (i.e. the product $b \cdot B_{fe}$) is fixed, the Ampere law defines the relationship (5) between the selected d-axis magnetizing loading and the required mmf F_d .

$$F_d = \frac{b \cdot B_{fe}}{\mu_0} g = \frac{B_{gap,d}}{\mu_0} g \quad (5)$$

Then, the d-axis electric loading A_d (6) is determined:

$$A_d = \frac{\pi}{2\mu_0} b \cdot B_{fe} \frac{g}{a} \quad (6)$$

A_d is proportional to the pu airgap g/a , to indicate that, when the airgap is too thick, a non-negligible part of the current loading is spent for d-excitation, with negative impact on the Joule loss and the PF, as it will be recalled in the following.

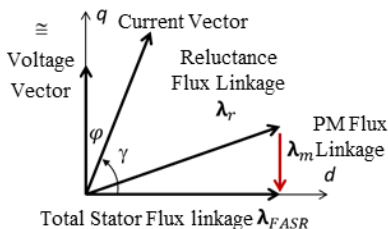


Fig. 4. Vector diagram of a “Naturally Compensated” PM-assisted machine.

B. Natural compensation of the q-axis flux-linkage

When dealing with PM-assisted motors, the magnets flux is designed for compensating either the whole q-axis flux of the basic SR machine or the majority of it [15]. In the former case, represented by the vector diagram of Fig. 4, the FASR machine is “naturally compensated” [1]. It says that:

- the PF is defined by the current argument only and just few poor design choices (i.e. the ones with large pu airgaps) lead to unsatisfactory PF values;
- the stator back iron is saturated primarily by the d-axis magnetizing flux and the cross saturation effects are definitely reduced.

“Natural Compensation” will be considered, from now on, as the rated design condition of the elementary block. In other words, the PM flux linkage λ_m will be designed for having the q-axis rated current of the machine equal to the characteristic (or short circuit) one, namely I_{q0} [18]. In formula:

$$\lambda_m = L_q I_{q0} \quad (7)$$

where L_q is the q-axis inductance.

The PM flux linkage λ_m of one rectified pole (8) is a function of the flux density $B_{gap,m}$, produced in the airgap by the magnets.

$$\lambda_m = \frac{2}{\pi} k_w N \cdot a \cdot l \cdot B_{gap,m} \quad (8)$$

The characteristic loading A_{q0} follows from (8), according to the definitions (4) and (7):

$$A_{q0} = \frac{3\pi}{4\mu_0} \cdot \frac{B_{gap,m}}{L_{q,pu}} \quad (9)$$

Where the normalization $L_{q,pu} = L_q / L_{base}$ is based on (10):

$$L_{base} = \mu_0 l \cdot \left(\frac{2}{\pi} \cdot k_w N \right)^2 \quad (10)$$

The key role played by A_{q0} has to do with the torque capability of the machine, as it will be demonstrated. Thus, it is worth pointing out its dependence on the main design parameters. It will be done by defining $B_{gap,m}$ and $L_{q,pu}$, in Subsection III.C and III.D, respectively.

C. PM and airgap flux density at no load

At no load, the peak flux density in the airgap $B_{gap,m}$ and the uniform flux density in the magnets B_{m0} are proportional to each other and are both obtained by solution of the magnetic circuit in Fig. 2.

The no load flux-density in the magnets, in pu of the PM remanence B_r , is derived in [12]. Its expression (11) is reported here for convenience, reminding that $l_{a,pu}$, which is equal to $l_a/(a/2)$, represents the rotor pu magnetic insulation.

$$\frac{B_{m0}}{B_r} = \left(1 + \frac{4\pi}{l_{a,pu}} \frac{S_1 \sin(\Delta\xi/2)}{a} \frac{g}{\Delta\xi} \frac{g}{a} \right)^{-1} \quad (11)$$

In (11), the term S_1/a can be simplified and the PMs volume, in pu of the rotor one, can be introduced instead. The substitution will lead to a more useful formulation, since the normalized PMs volume ($V_{m,pu}$) is known to be an indicative design indicator, strictly correlated to the chosen $l_{a,pu}$.

The relationship between S_l/a and $V_{m,pu}$ is solved, as shown by (12), considering the geometrical constraints fixed by (2) and (3) on the magnets lengths and widths.

$$V_{m,pu} = \frac{4(S_1 l_1 + \dots + S_n l_n) \cdot l}{a^2 \cdot l} = \frac{n_r l_{a,pu}}{2} \frac{\tan(\Delta\xi/2) S_1}{\cos(\Delta\xi/2) a} \quad (12)$$

Then, Equation (13) is obtained by substituting (12) into (11) and by approximating the trigonometric function $\cos(\Delta\xi/2)$ with the first two terms of the respective Taylor series. The parameter n_r is put in evidence by means of (1).

$$\frac{B_{m0}}{B_r} \cong \left(1 + \frac{4 \cdot V_{m,pu}}{l_{a,pu}^2} \left(1 - \frac{\pi^2}{n_r^2} \right) \frac{g}{a} \right)^{-1} \quad (13)$$

The PMs flux density B_{m0} (13) at no load:

- determines the robustness of the machine towards demagnetization at any operating conditions, as it will be demonstrated later;
- defines the no load flux density in the airgap via a proportional relationship, that will be introduced in the following.

The maximization of B_{m0} has then a twofold purpose, that, according to (13), can be better pursued when dealing with multi-layer rotor structures ($n_r \geq 14$), as the ones considered here. Equation (13) also suggests that designs with thick pu airgaps g/a and small rotor magnetic insulation $l_{a,pu}$ penalize the no load flux density in the magnets. Recommended values of $l_{a,pu}$ are around 0.35-0.45. With larger pu insulation, the design of the rotor flux guides would be poor and the consequent iron saturation effects might compromise the machine performance.

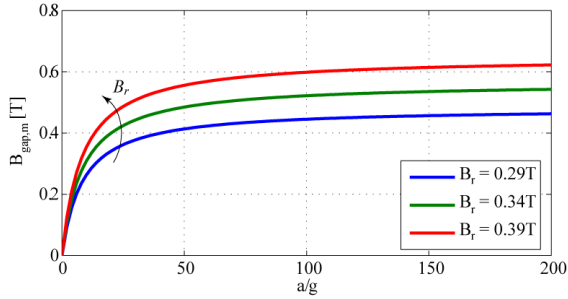


Fig. 5. Peak flux density in the airgap at no load (14), as a function of the pole pitch to airgap ratio. Ferrite grades with different remanence values are shown. The example is for $l_{a,pu} = 0.4$, $V_{m,pu} = 0.35$, $n = 3$, $n_r = 14$.

As said, a proportional relationship (14) between the airgap flux density and the PMs one can be found from the q-axis magnetic circuit of Fig. 2:

$$B_{gap,m} = \frac{V_{m,pu}}{l_{a,pu}} \frac{\Delta\xi \cdot \cos(\Delta\xi/2)}{\tan(\Delta\xi/2)} B_{m0} \cong 2 \frac{V_{m,pu}}{l_{a,pu}} \left(1 - \frac{\pi^2}{n_r^2} \right) B_{m0} \quad (14)$$

The previous equation accounts for the flux concentration effect of this type of PM machines. If the FASR rotor is designed with proper values of both $l_{a,pu}$ (e.g. 0.35-0.45) and $V_{m,pu}$ (e.g. 0.3-0.4), the airgap flux density $B_{gap,m}$ results to be roughly 2 times the flux-density in the magnets. The flux density in the magnets, in turn, can be optimized as described. That is to say that low energy density PMs can still produce a valuable flux density in the airgap, thanks to the particular

rotor topology. Once more, multi-layer rotor structures (i.e. $n_r \geq 14$, $n \geq 3$) show noticeable advantages. In fact, in case of more standard IPM machines with one or two layers (that is, lower n_r values) the flux concentration is penalized by the terms in bracket in (14).

Fig. 5, which puts together (13) and (14), shows the peak flux density produced by the PMs in the airgap, as a function of a/g and the magnets grade. The plots are referred to the room temperature. However, the actual temperature of the PMs and the law of degradation of their B-H characteristic with the temperature affect $B_{gap,m}$, and this dependence has to be taken into account in the design procedure.

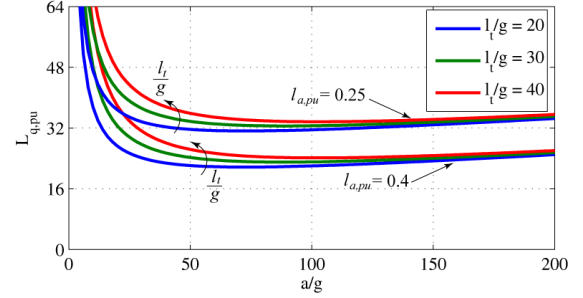


Fig. 6. Per unit q-axis inductance as a function of the pole pitch to airgap ratio and with the pu tooth length l_t/g as a parameter. $L_{q,pu}$ is shown in correspondence of both an inadequate (0.25) and an adequate (0.4) value of $l_{a,pu}$. Other parameters: $q = 3$, $n = 3$, $n_r = 14$, $k_w = 0.96$, $b = 0.55$, $k_t = 0.9$, $k_{tip} = 1.4$.

D. q-axis inductance and its component

When designing PM-assisted motors, the minimization of the q-axis inductance is one pivotal aspect, as it improves the rotor saliency of the basic SR machine. Besides, with low L_q values, the PM flux linkage needed to fulfill the natural compensation condition (9) can be reduced, or, if the PMs grade and volume are given, the characteristic current (7) can be increased.

The total q-axis inductance accounts for the magnetizing term $L_{m,q}$ (15), the slot leakage one $L_{\sigma,slot}$ (16) and the zig-zag inductance $L_{zz,q}$ (17).

$$L_{m,q} = \frac{3\pi^2}{4l_{a,pu}} \left(1 - \frac{2}{n_r} \right) L_{base} \quad (15)$$

$$L_{\sigma,slot} = \frac{\pi^2}{2k_w^2 (1 - bk_t)} \cdot \frac{l_t}{g} \cdot \frac{g}{a} \cdot k_{tip} \cdot L_{base} \quad (16)$$

$$L_{zz,q} = \frac{1}{8} \left[\left(\frac{\pi}{3q} \right)^2 + \left(\frac{2\pi}{n_r} \right)^2 \right] \cdot \frac{a}{g} \cdot L_{base} \quad (17)$$

More details about (15) can be found in [15]. Equation (16) is presented in its simplest version [19]-[20], as a more complicate one is needed for including the case of chorded windings. In (16), l_t is the tooth length, $(1 - bk_t)$ is representative of the slot width and k_{tip} quantifies the inductance increase of a semi-closed slot with respect to an open one, due to the tooth tip shoe. The zig-zag inductance [21], as highlighted by the squared terms in round brackets in (17), includes both the stator and rotor slots leakage effects, being q the number of stator slots per pole per phase.

The curves reported in Fig. 6 put in evidence that for small values of a/g the slot leakage component dominates the total q-axis inductance with a bad impact on the achievable saliency ratio. Conversely, starting from a/g values roughly larger than 50, the term $L_{\sigma,slot}$, and thus the choice of l_t/g , get increasingly less important in affecting the total q-axis inductance. This value is definitely determined by the magnetizing component, especially when the zig-zag one is small thanks to high q and n_r values. It points out that both the p.u. insulation $l_{a,pu}$ and the parameter n_r (i.e. the number of layers) are of crucial importance for the minimization of the overall q-axis inductance.

E. Characteristic electric loading

The characteristic electric loading is directly proportional to $B_{gap,m}$ (Fig. 5) and inversely proportional to $L_{q,pu}$ (Fig. 6). As a result, the A_{q0} curves in Fig. 7 are flat in a wide range of a/g . In the same range (that is, $50 \leq a/g \leq 200$) the tooth length factor (l_t/g) is not of great importance, whereas the magnet grade, expectedly, is. Also the pu magnetic insulation in the rotor and the normalized PMs volume affect the characteristic current loading. As an example, the plots in Fig. 7a show the behavior of A_{q0} , referred to the outer values of typical $l_{a,pu}$ and $V_{m,pu}$ design spaces. In particular, larger magnetic insulations and, consequently, larger PMs volumes are distinctive of multipolar machines, since the shape of their poles, closer to the rectified one, is more convenient to optimize simultaneously the design of the rotor flux barriers and iron guides.

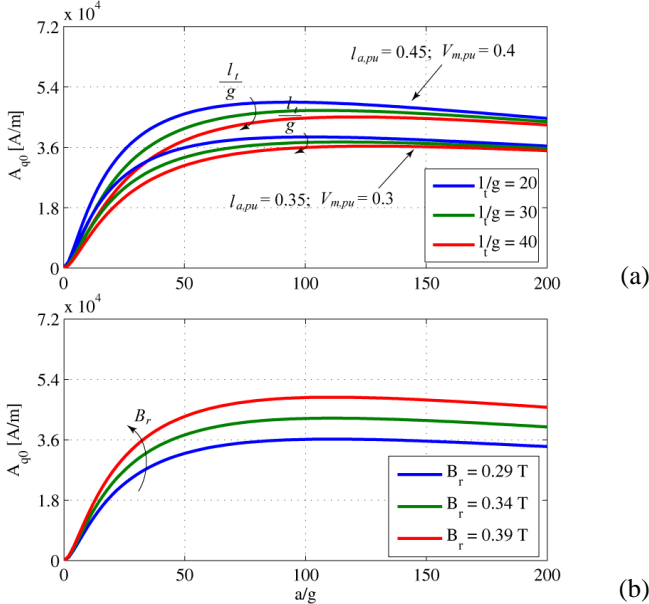


Fig. 7. Characteristic electric loading. Design inputs: $q = 3$, $n = 3$, $n_r = 14$, $k_w = 0.96$, $b = 0.55$, $k_t = 0.9$, $k_{ip} = 1.4$. a) Effect of l_t/g , $l_{a,pu}$ and $V_{m,pu}$, with $B_r = 0.34$ T. b) Effect of B_r with $l_t/g = 30$, $l_{a,pu} = 0.4$ and $V_{m,pu} = 0.35$.

F. Accuracy of the model

The accuracy of the proposed analysis can be improved as suggested in the Appendix:

- Appendix A illustrates how to take into account the presence of rotor structural bridges, by quantifying the reduction of the PMs flux concentration effect (14).

- Appendix B enlists the equations needed for modifying the definition of the d-axis current loading (6), so to compensate for the magnetic potential drops in the saturated stator back iron.

The effectiveness of the formulas reported in the Appendix will be discussed in the last Section, by comparing the results of the proposed model to the experimental data.

IV. PERFORMANCE INDICATORS

A. Shear stress

The shear stress [Nm/m³], averaged over one machine pole, is the cross product (18) of the airgap flux density by the electric loading [19].

$$\sigma = B_{gap,d} A_q - B_{gap,q} A_d \quad (18)$$

In the area that has been revealing of main interest for the design (i.e. $50 \leq a/g \leq 200$), if the machine is “naturally compensated”, the second term of (18) is negligible, because both $B_{gap,q}$ and A_d are significantly smaller than the respective counterparts on the other axis. Thus, the characteristic shear stress σ_0 is approximately defined as in (19):

$$\sigma_0 \cong B_{gap,d} A_{q0} = b B_{fe} \cdot A_{q0} \quad (19)$$

where the subscript 0 reminds of the reference to the “Natural Compensation” condition.

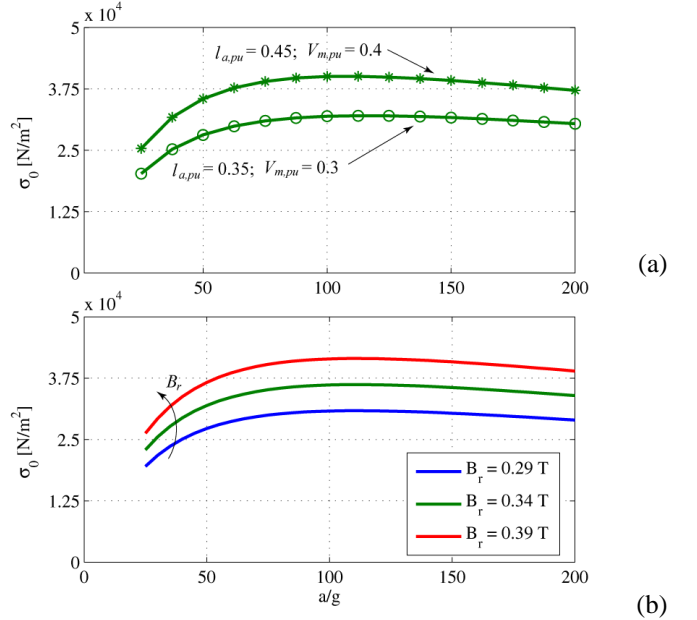


Fig. 8. Characteristic shear stress, for the same design inputs declared in Fig. 7. l_t/g is fixed and equal to 30. All the σ_0 curves are plotted starting from $a/g = 25$, since for lower a/g values the approximation (19) is too imprecise. a) σ_0 is referred to the outer values of typical $l_{a,pu}$ and $V_{m,pu}$ design spaces. ($B_r = 0.34$ T); b) Effect of B_r with $l_{a,pu} = 0.4$ and $V_{m,pu} = 0.35$.

Given the d-axis magnetic loading $B_{gap,d}$, the shear stress is decided by the characteristic loading only. As a consequence, it is influenced by: the pole pitch to airgap ratio a/g , the rotor pu insulation, the magnets volume and remanence. The curves in Fig. 8 quantify the impact of these four design parameters on the achievable performance, highlighting that the shear stress figures are competitive with the ones of Nd-based

machines [19], [22] especially for designs with large pu rotor insulation and multi-layer rotor structures. In that cases, A_{q0} is maximized thanks to the low q-axis inductance and the valuable concentration of the PMs flux in the airgap. This, associated to good ferrite grades improves the torque capability of the machine. Or, at given torque, it allows the employment of lower energy density magnets, since, being the layers completely filled with ferrite, their quantity is fixed.

To deal with shear stress values typical of very large liquid cooled machines, the analysis can be extended to “non-naturally compensated” machines, taking advantage of the better cooling system to put into play q-axis electric loadings larger than A_{q0} and thus increase the achievable σ .

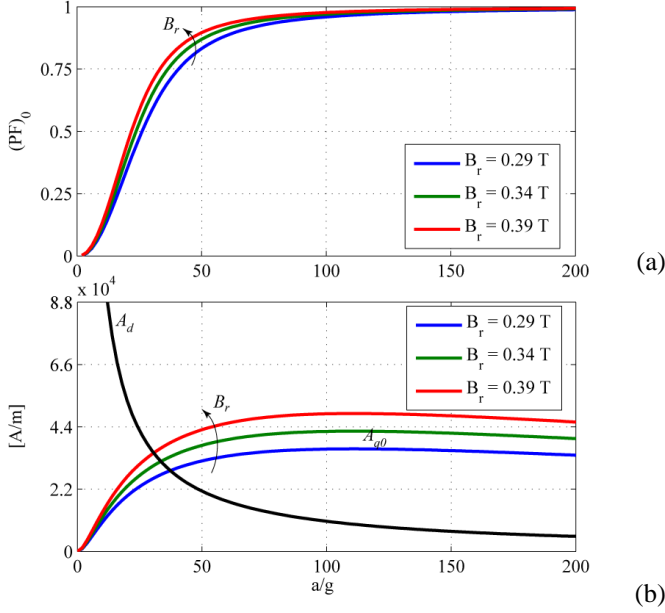


Fig. 9. PF (top) and current loading components (bottom) at “Natural Compensation” as functions of the pole pitch to airgap ratio and the PM grade. Same design parameters as in Fig. 7 and 8 ($l/g = 30$, $l_{a,pu} = 0.4$ and $V_{m,pu} = 0.35$).

B. Power factor of “Naturally Compensated” machines

Disregarding the resistive voltage drop as indicated in Fig. 4, the PF angle φ_0 (20) at “Natural Compensation” is defined by the current phase angle only:

$$\tan(\varphi_0) = \tan\left(\frac{\pi}{2} - \gamma\right) = \frac{A_d}{A_{q0}} \quad (20)$$

As shown in Fig. 9, both A_d and A_{q0} penalize the PF in the low range of a/g . But, as a/g increases, the PF tends asymptotically to one, whatever the PMs. In other words, the pu airgap g/a (that is, the choice of the pole pairs in the final design) is the only variable to influence the PF of “Naturally Compensated” FASR machines.

C. Stiffness towards demagnetization

Regarding demagnetization issues, the main figure of merit is the maximum feasible q-current loading $A_{q,irr}$, that is the one that takes the PMs to the edge of irreversible demagnetization.

$$A_{q,irr} = \frac{\pi}{4} \frac{B_r l_{a,pu}}{\mu_0 f_{qn}} \left(1 - \frac{B_{m,irr,pu}}{B_{m0,pu}}\right) \quad (21)$$

$$B_{m,irr,pu} = \frac{B_{m,knee}}{B_r} \quad (22)$$

Equation (21) is derived from the magnetic circuit of Fig. 2 [12]. It introduces the knee of demagnetization $B_{m,irr,pu}$, defined by (22), in pu of the PMs grade, and points out that, besides the per-unit insulation, also the PMs flux density at no load has to be as high as possible to maximize $A_{q,irr}$. In fact, if $B_{m0,pu}$ gets closer to the knee of demagnetization, no room for the current loading is left and the magnets can be damaged even at no load. It follows that, according to (13), the need of designing the rotor as a multi-layer structure with good magnetic insulation along the q-axis is again well documented, as highlighted in subsection III.C.

Another factor that plays a key role in (21) is the operating temperature, that affects both the remanence flux density and the knee of irreversible demagnetization, as shown in the example B-H curves of Fig10. However, when dealing with very cold environments, if the demagnetization issues result to be critical, even with $B_{m0,pu}$ maximized via optimized rotor designs, specialized ferrite grades with low $B_{m,knee}$ at all practical temperatures can be found [23].

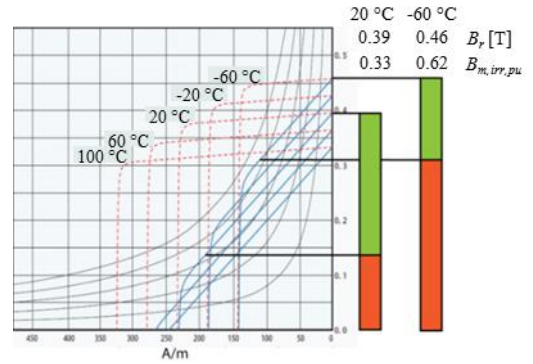


Fig. 10. Magnetic curves of Hitachi Ferrite grade NMF-3C, and graphical expression of the $B_{m,irr,pu}$ at -60°C and 20°C.

D. Joule loss density

The Joule loss density of the rectified pole of Fig.1, referred to the block surface ($a \cdot l$), is:

$$k_{j,block} = 2\rho_{Cu} \cdot \frac{k_{end}}{k_{Cu}} \cdot \frac{1 - bk_t}{l_t} \cdot \frac{A_d^2 + A_q^2}{k_w^2} \quad (23)$$

Where ρ_{Cu} is the copper resistivity, k_{Cu} is the slot filling factor and k_{end} is the total length of one conductor, end connections included, in pu of the active length,

Since core and PM losses can be disregarded in this analysis, which is dedicated to low speed multipolar machines, the Joule loss density is representative of both the efficiency and the type of cooling of the machine. Regarding the efficiency, the key role played by the tooth length is put in evidence in (23). However, as l_t heavily affects also the mass of active materials of each pole, a tradeoff must be found. Equation (23) can be used also to find out the maximum electric loading A_{th} ($= [A_d^2 + A_q^2]^2$) at rated thermal conditions, considering that the type of cooling identifies a maximum value for the heat rate density. The thermal limit A_{th} must be

compatible with the other key values of electric loading A_d , A_{q0} and $A_{q,irr}$, as discussed in [12].

E. Summary of the elementary block analysis

From the analysis of the rectified block it turns out that:

1. Designing multi-layer structures with good insulation properties improves the stiffness against demagnetization. It allows also to minimize the q-axis inductance and maximize the magnetic loading produced by the PMs, by concentrating the flux in the airgap. This is twice beneficial for the shear stress.
2. Given both n_r and l_{apu} , low pole pitch to airgap ratios a/g , meaning thick pu airgaps, make the machine prone to demagnetization and reduce the magnetic loading obtainable in the airgap thanks to the magnets. If a/g is too small, also the saliency ratio is unsatisfactory. In particular, the magnetizing d-axis inductance is low (requiring high excitation currents), whereas the q-axis one is high (badly affecting the characteristic electric loading).
3. From the previous point, it follows that a low a/g ratio is a symptom of low shear stress, low PF and low efficiency (or more specifically increased Joule losses).
4. The characteristic shear stress depends significantly on the PMs remanence, and very little on the stator tooth length, which will be handled as an important degree of freedom in the final design of the rotating machine. It impacts the machine weight, besides its efficiency.

V. ROTATING MACHINE INTO CONSTRAINED ENVELOPE

A rotating machine, that is defined by the input data in Table II, can be seen as an assembly of $2p$ elementary blocks, all having the rotor pitch equal to a . Thus, given the target torque T , the stack outer radius (r) and length (l), the machine can be designed via the closed form equations presented in the previous subsection. All the normalized parameters required to start the design have already been discussed and are briefly summarized in Table II. The design variables are: the pole pairs number p and the tooth length l_t .

Both p and l_t contribute to define the rotor radius r' (24). This is also due to the dependence, shown in Fig. 1, of the stator yoke height on the rotor pole pitch a , which, in turn, is identified by (25), and thus again by p and l_t .

$$r' = r - l_t - l_y \rightarrow r' = r \frac{1 - \frac{l_t}{r}}{1 + \frac{b}{p}} \quad (24)$$

$$a = \frac{r'}{p} \pi \quad (25)$$

Given the torque, the relationship (24) allows to express the required shear stress (26) in terms of the variables l_t/r and p .

$$\sigma = \frac{T}{2\pi \cdot (r')^2 \cdot l} \quad (26)$$

Then, if the desired magnetizing loading $b \cdot B_{fe}$ is provided by a correct choice of the d-axis current loading (6), the characteristic q-axis electric loading follows directly from (26) by inversion of (19). As a result, both A_d and A_{q0} turn out to be

functions of the variables p and l_t/r . And the same is for the PF (20) and the PM grade needed for “Natural Compensation”, which can be derived via (9)-(13) starting from the A_{q0} value. Also the Joule loss density k_j can be easily computed as a function of the other design quantities, keeping in mind that the heat rate density is here reasonably calculated here at the outside surface and is then related to the block one by (27).

$$k_j = k_{j,block} \cdot \frac{r'}{r} \quad (27)$$

The proposed procedure can be iteratively applied in order to explore all the feasible combinations of l_t/r and p , that give the desired torque with the stack envelope constrained. The design spaces of the two variables are identified in Subsection V.A and the concurrent designs are compared in Subsection V.B, so to derive general guidelines for optimized solutions. In particular, Subsection V.C shows how to simplify the design task, if the Joule loss density needs to be minimized. In that case, an analytical expression fixes the optimal pole pairs number, which does exist due to the different variation of the d- and q-axis current loadings with p . In fact:

- as p increases, the rotor pitch a gets smaller and the d-axis current (6), needed to have the airgap flux density equal to $b \cdot B_{fe}$, increases;
- as p decreases, the bore radius decreases, as shown by (24)-(25). It means that the lever associated to the airgap shear stress is reduced and greater q-axis currents (26) are required. Also the end connections are longer if the bore radius is smaller, with a bad impact on the resulting k_j .

TABLE II
DESIGN PROCEDURE: MAIN PARAMETERS, INPUT AND OUTPUT DATA

Input data	
Geometrical quantities	r, l, g
Performance target	Torque T
Design parameters	
Magnetizing loading and sizing of the stator back iron	b, B_{fe}, k_t
Rotor design	$n_r, n, l_{apu}, V_{m,pu}$
Stator winding design	$q, k_{ws}, k_{Cus}, k_{end}$
Design variables	
Pole pairs p and stator tooth length l_t	
Performance indicators and other design outputs	
Needed PM grade B_r , Electric loadings A_d and A_{q0} , PF, Joule loss density k_j	

A. Upper and lower limits to the design variables

The choice of the tooth length factor l_t/r is a matter of trade-off, as it affects both the efficiency of the machine and the weight of its active materials. According to (23), too short stator teeth lead to unfeasible designs due to the increased Joule loss. On the other hand, having too long teeth impacts negatively the total weight, in addition to other unwanted side effects. In particular, with longer teeth and consequently smaller bore radius, the lever associated to the airgap shear stress is reduced and higher q-axis current loadings are required, at given output torque. Also the length of the end connection grows with l_t/r and it contributes to vanish the convenience of increasing the tooth length, over a certain extent, to reduce the Joule loss. As a result, effective l_t/r design spaces typically include values that vary from few percent to 25%, also depending also on the machine size.

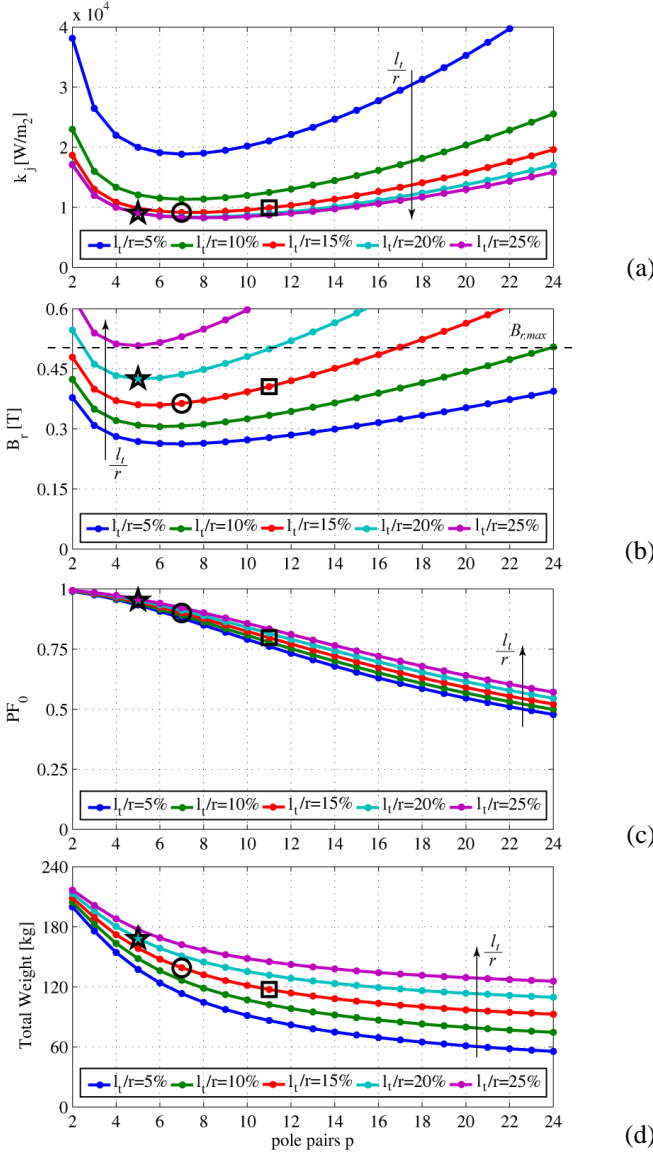


Fig. 12. Prototyped direct drive lift motor ($T = 795$ Nm, $r = 0.19$ m, $l = 0.25$ m, $b \cdot B_{fe} = 0.84$ T). The plots show the Joule loss density (a), PM remanence (b), PF (c) and total machine weight (d) as function of the number of pole pairs and with the tooth length as a parameter. Three different designs are compared: the “circle” design is for Joule loss minimization; the “star” design is similar to the former one, but has longer stator teeth; the “square” design is for weight reduction.

The analysis on the reference block suggests the presence of a lower limitation for a/g ($a/g \geq 50$) and thus an upper limit for the pole pairs number. In order to quantify it, Equation (28) is derived from (24) and (25).

$$p_{max} = \pi \frac{r}{g} \left(\frac{a}{g} \bigg|_{min} \right)^{-1} \left(1 - \frac{l_t}{r} \right) - b \quad (28)$$

In (28) the parameters b and l_t/r can be defined as discussed, then the minimum recommended a/g value univocally identifies the maximum number of pole pairs. This upper limitation, which is compliant with the core loss minimization purposes, depends on r/g . In turn, the ratio r/g , mainly related to constructional aspects, is a function of the machine size: it can be around 100, when dealing with small traction motors, and raise up to 500, for large wind turbine

generators. A lower limit to the pole pairs number does also exist, because, as said, when p decreases, the yoke height increases and the bore radius, together with the torque lever, decrease. It follows that machines with too few poles are heavier and less efficient, because of the augmented q-axis electric loading.

B. Concurrent designs at given torque and outer stack

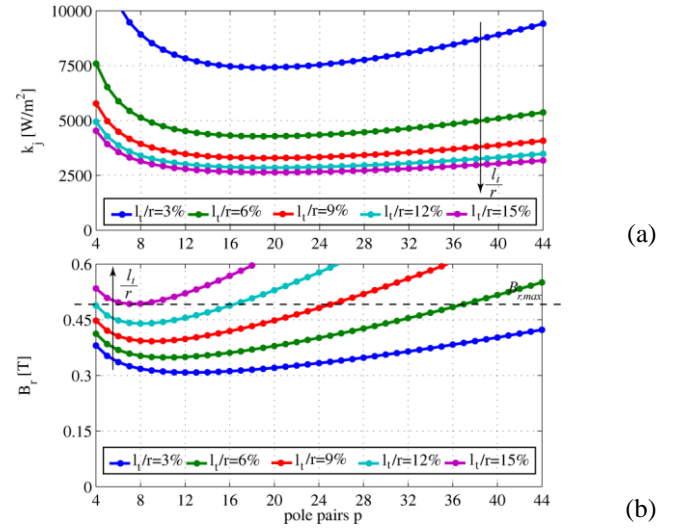
For finding out the best combinations of p and l_t/r with respect to the main design indicators, two examples are considered. The first one is the direct drive lift motor tested to validate the proposed analysis. It is rated 14 kW at 168 rpm; its outer radius is 0.19 m, its stack 0.25 m, its airgap length 0.75 mm. The other design example is a wind generator, rated 2 MW at 15 rpm. Its outer radius is 2 m, its stack 1.5 m and its airgap length 4 mm. The two machines have been purposely chosen, since they are very different in terms of required shear stress, size and shape of the stack (specifically, r/l ratio).

(a)

(b)

(c)

(d)



(a)

(b)

Fig. 13. Wind turbine generator ($T = 1273$ kNm, $r = 2$ m, $l = 1.5$ m, $b \cdot B_{fe} = 0.85$ T). The plots show the Joule loss density (a) and PM remanence as functions of the pole pairs number and with the tooth length as a parameter.

The curves in Fig. 12 refer to the prototyped motor, showing the charts of the Joule loss density, the needed PMs grade, the PF and the total weight, as functions of the pole pairs number and with l_t/r as a parameter. Fig. 12a highlights that the Joule loss density is always minimum in correspondence of a specific number of pole pairs, that does not depend on the tooth length. It is also evident that the loss reduction obtainable by lengthening the stator teeth flattens with l_t/r beyond 15%. It says that, in this case, a machine with p equal to 7 and l_t/r lower than 15% (that is, the “circle” design in Fig. 12) results the most convenient in terms of Joule loss minimization. Conversely, the values of p that minimize the ferrite remanence needed to fulfill the “Natural Compensation” condition vary with respect to the tooth length, as shown by Fig. 12b. In general, with longer stator teeth, the required PM grade is higher and more sensitive to the number of poles. For example, the “star” symbol in Fig. 12 indicates a design with $p = 5$ and $l_t/r = 20\%$, that has nearly the same loss of the “circle” design but needs $B_r = 0.43$ T instead of 0.37 T. From Fig. 12c and Fig. 12d, it is highlighted that the choice of

the pole pairs number is critical for both the PF and the total weight of the machine. However, the PF is good (meaning, higher than 0.85) for both the “star” and “circle” designs. Mass reduction could lead to consider a number of pole pairs larger than 7, for example $p=11$ (that is, the “square” design), but it would require to accept a lower efficiency, a better PM grade, a poorer PF and a higher fundamental frequency with the need of a proper check on the iron loss, up to now disregarded.

Fig 13, that refers to the large wind generator, confirms the qualitative considerations presented for the prototyped lift motor, highlighting the generality of the proposed approach. The PF and weight curves are not reported for brevity. Anyway it can be pointed out that the PF is even less critical in this case. The number of the pole pairs that minimize the Joule loss density here is very different from the one found for the previous design example, since, as it will be demonstrated in the next subsection, this value is strictly related to the machine size and required torque.

C. Optimal pole pairs number for Joule loss minimization

The number of pole pairs p_o (29), that minimizes the Joule loss, can be expressed analytically, if (27) is minimized, reminding (23) and applying the proposed procedure to write both A_d and A_{q0} as functions of the two design variables.

$$p_o = \sqrt[3]{\frac{3}{2} \left(1 + \frac{\pi k_{sh} r}{3b} \frac{1 - \frac{l_t}{2r}}{1 - \frac{2l_t}{l}} \right) \left(\frac{1}{1 - \frac{l_t}{r}} \frac{\mu_0}{b B_{fe}} \frac{r}{g} TSV \right)^2} \quad (29)$$

In (29), the torque density TSV is referred to the stator volume and k_{sh} is the winding shortening factor, which is lower than one only in case of chorded windings.

Equation (29) can be simplified, obtaining (30), with very little loss of accuracy, especially when the factors l/r and l_t/l are small, as it is for large size generators.

$$p_o \cong \sqrt[3]{\frac{3}{2} \left(b + \frac{\pi}{3} k_{sh} \cdot \frac{r}{l} \right) \cdot \left(\frac{\mu_0}{b B_{fe}} \frac{r}{g} TSV \right)^2} \quad (30)$$

Equation (30) puts in evidence that p_o depends on:

- the outer radius to length ratio r/l , representative of the shape of the stack;
- the outer radius to airgap ratio r/g , accounting for the machine size and mechanical aspects;
- the torque density per stator volume TSV , again related to the machine size and to the type of cooling.

In general, pancake shape (i.e. $r/l \gg 1$), small per unit airgap and high TSV are all factors leading to increase the optimal number of poles for Joule loss minimization. This is quantified by (30) and confirmed by the examples examined in the previous subsection. In fact, if compared to the prototyped lift motor, the wind generator has a TSV that is increased by 2.4 times, a double r/g value and a r/l ratio increased by 1.33. Then, also the optimal pole pairs number shifts from 7 to nearly 20, as graphically represented by Fig. 12a and Fig. 13a.

VI. FEA AND EXPERIMENTAL RESULTS

A. FASR prototypes and experimental setup

Two twin motors for lift application were prototyped, on the basis of the specifications discussed in the previous section.



Fig. 14. Twin FASR prototypes, shaft connected on the test rig.

TABLE III
DESIGN PARAMETERS, GEOMETRICAL INPUTS AND OUTPUTS.

Design Parameters		Input data	
Yoke per-unit width b	0.54	Torque T	795 Nm
Back-iron flux density B_{fe}	1.55 T	Nominal Speed	168 rpm
Tooth width factor k_t	0.92	Stator diameter $2r$	380 mm
Rotor slots per pole pair n_r	14	Active Length l	250 mm
Rotor flux barriers n	3	Airgap length g	0.75 mm
Pu rotor insulation $I_{a,pu}$	0.42	Geometrical design outputs	
Pu magnets volume $V_{m,pu}$	0.30	Pole pairs p	7
Slot per pole per phase q	3	Pu tooth length l_t/r	14.4 %
Winding factor k_w	0.96	Rotor diameter $2r'$	296.5 mm
End connections factor k_{end}	1.53	Other outputs	
Slot filling factor k_{Cu}	0.4	PMs remanence B_r	0.37 T

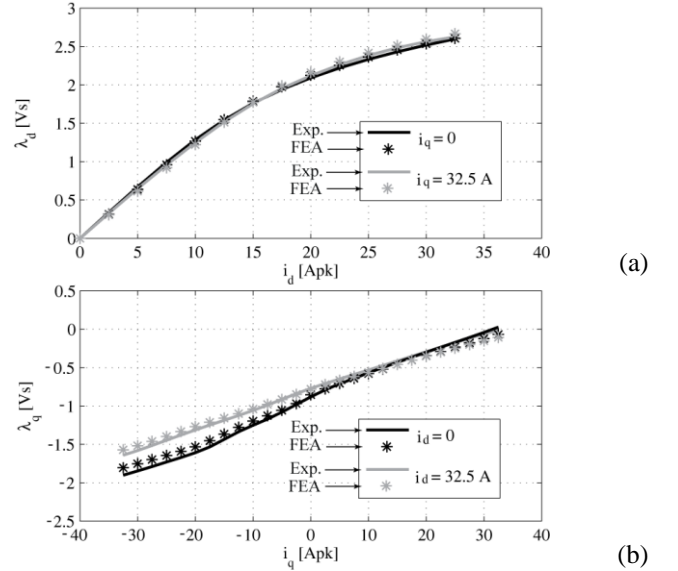


Fig. 15. d- and q-axis stator flux linkages of the twin prototypes of Fig. 14. Both the FEA results and the experimental data refer to a stabilized value of the operating PMs temperature (that is, 100°C).

The prototypes are “Naturally Compensated” FASR machines, designed with a number of pole pairs equal to p_o (30) in order to minimize the Joule loss (that is, the “circle” design in Fig. 12). The main input data, normalized parameters and outputs of the design are reported in Table III. The magnet grade B_r needed to fulfill the “Natural Compensation” condition has been evaluated taking into account the effect of the rotor structural bridges, that reduce the concentration of the PMs flux linkage by 16%, in this case

(Appendix A).

During the tests, the two prototypes were shaft connected, as shown in Fig. 14, and the respective converters were back to back connected, with the dc-link in common. A torque-meter (HBM-T40B) was interposed and two power analyzers (Zimmer-LMG500) were used to log the electric quantities at the two machines' terminals. Continuous operation was tested, with the direct measurement of the stator temperatures (windings, chassis) and the estimation of the PMs ones via back-emf measurement.

The flux linkage curves (Fig 15) and the torque one (Fig.16) have been identified over the (i_d, i_q) plane, following the experimental procedure introduced in [24]. The results of Fig. 15 show that both the d- and q-axis flux linkages are just merely affected by the current on the heteronymous axis, at least in the area of interest for the control (that is, $i_q \geq 0$). Especially for the d-axis flux linkages, it occurs thanks to the choice of "Natural Compensation". So the experimental results confirms the theoretical discussion. In Fig. 15, the 2D FEA flux linkages do match quite well the experimental ones. The leakage fluxes in the cast iron stator chassis are not negligible in this case and they were included in the FE model. The end connections flux linkages are small, if compared to the other contributes, and were not modeled. Anyway, as all the leakage fluxes do not contribute to produce the torque, the accordance between FEA and experiment is always good, when comparing the torque, as done in Fig 16 at given current amplitudes and variable current arguments.

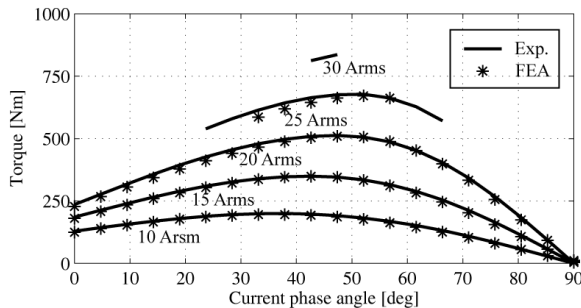


Fig. 16. Torque curves of the twin prototypes of Fig. 14 at constant current amplitude and variable phase angle. Both the FEA results and the experimental data refer to a stabilized value of the operating PMs temperature (that is, 100°C).

TABLE IV
EXPERIMENTS, FEA AND MODEL: COMPARISON OF THE RESULTS

Quantity	Exp.	FEA	Model	
Torque	791	799	795	Nm
Current	28.3		28.3	A rms
Current phase angle	53.3		61.0	degree
PM-flux (20°C)	1.0	1.0	0.99	Vs
d-flux	2.34	2.36	2.33	Vs
q-flux	-0.01	-0.015	0	Vs
Line Voltage	230	-	-	Vrms
Joule loss	2660	-	3134	W
Copper temperature		100		°C
Power Factor	0.85	0.87	0.87	
Core loss (stator + rotor)	300	-	-	W
Loss density - Joule (k_j)	8980	-	10500	W/m ²
Loss density - Total (k_t)	9988	-	10500	W/m ²

B. Validation if the adopted analytical model

A detailed list of the results produced by the adopted model

is reported in Table IV, for a fair comparison to the experimental and FEA data. As it can be seen, a very good matching has been obtained between experimental and model results, except for the optimal current phase angle and the expected Joule loss. The former is underestimated by the model, as the core saturation effects contribute to modify the Maximum Torque Per Ampere (MTPA) locus in the (i_d, i_q) plane. However, it is worth pointing out that the current amplitude, needed to produce the willed torque, is predicted with good accuracy. This is also thanks to the corrective factor proposed in Appendix B for the d-axis current loading. It attempts to compensate for the stator back iron magnetic potential drops increasing A_d by 14%. On the contrary, the model overestimates the Joule loss, because of the rectified geometry, which schematically models parallel side slots, referring their constant widths to the (shorter) bore radius. Anyway, the model estimation results "safer" from this point of view. This is valid for the prototypes under test, even if the additional core losses are considered. Their measured value is reported in Table IV.

In Table IV the FEA results are reported as well, for completeness. Their agreement with the experiment looks reasonably good, according to what already discussed about the stator flux linkages and the need of modeling the effect of the cast iron chassis (Fig. 15).

VII. CONCLUSION

A general approach to the optimal design of multipolar FASR machines has been discussed. The procedure is based on a fully analytical per-unit model, that has a twofold purpose. First, it aims at orienting the designers to the most convenient solutions by means of general guidelines, suitable for machines of all sizes and applications. Then, it provides closed-form equations to determine all the design variables and performance indicators of the machine. As a result, the FEA is not mandatory, but just useful for final refinements. In particular, a simple formula suggests the optimal pole pairs number to be adopted if the machine efficiency needs to be maximized, greatly simplifying the design task. In order to prove the generality of the design approach, the proposed method has been validated on different cases and, as an example, the paper refers to a direct-drive lift motor prototype and presents the experimental and FEA results, together with the model outputs. All the data are in good accordance, despite the simple nature of the adopted model.

APPENDIX

A. Appendix A

Rotor structural bridges shunt a portion of the PM flux, weakening the no load flux density in the airgap. As deeper explained in [4], their magnetic behavior can be modeled by the Norton equivalent circuit of Fig. 17, where the parameters $\Phi_{rib,k}$ and $p_{rib,k}$ depend on:

- the rib working point on the saturated B-H curve of the rotor iron (namely, the flux density B_R and the respective relative permeability μ_R);

- the rib thickness $S_{rib,k}$ and length, which can be expressed in pu of the respective barrier length via the factor k_{rib} .

With some manipulations, the superposition of the magnets model and the ribs one can be seen as its Thevenin equivalent, that has again the form of a PM-generated mmf m_k^* and an equivalent permeance p_{bk}^* , as the barrier circuit introduced in Fig. 2.

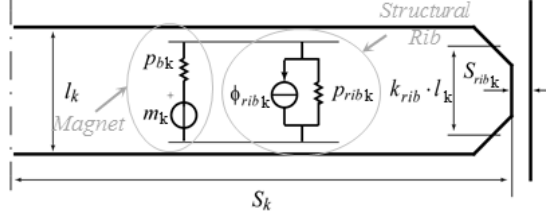


Fig. 17 Circuitual model with structural bridges included.

As a result, when it is needed to quantify the reduction of the PM flux due to the rotor structural ribs, it is sufficient to write the equations derived in Subsection III.C for finding out the no load flux density $B_{gap,m}$ substituting S_l with S_l^* (31) and B_r with B_r^* (32).

$$S_1^* = S_1 + \frac{\mu_R}{k_{rib}} S_{rib,1} \quad (31)$$

$$B_r^* = B_r \frac{S_1 - \frac{B_r}{B_r} S_{rib,1}}{S_1^*} \quad (32)$$

B. Appendix B

The magnetic potential drops associated to the flow of the d-axis flux in the stator back iron can be compensated, if the magnetizing current loading A_d (6) is increased by k_{sat} (33):

$$k_{sat} = 1 + \frac{1}{b} \cdot \frac{\frac{1}{k_t} \frac{l_t}{g} + \frac{1}{2} \left(1 - \frac{2}{\pi}\right) \frac{a}{g}}{\mu_0 \mu_{fe}} \quad (33)$$

μ_{fe} is the iron relative permeability in correspondence of the working flux density B_{fe} . B_{fe} is typically chosen to be around 1.5-1.7 T and the related μ_{fe} values are in the range of 600-800.

ACKNOWLEDGMENT

The authors are grateful to Sicme Motori s.r.l., for the experimental facilities.

REFERENCES

- [1] Moghaddam, R.R.; Magnussen, F.; Sadarangani, C.; , "Theoretical and Experimental Reevaluation of Synchronous Reluctance Machine," *Industrial Electronics, IEEE Transactions on* , vol.57, no.1, pp.6-13, Jan. 2010.
- [2] RR Moghaddam, "Rotor for a Synchronous Reluctance Machine", US Patent App. 13/230,543, 2011.
- [3] Barcaro, M.; Bianchi, N.; Magnussen, F., "Permanent-Magnet Optimization in Permanent-Magnet-Assisted Synchronous Reluctance Motor for a Wide Constant-Power Speed Range," *Industrial Electronics, IEEE Transactions on* , vol.59, no.6, pp.2495-2502, June 2012.
- [4] Guglielmi, P.; Boazzo, B.; Armando, E.; Pellegrino, G.; Vagati, A.; , "Permanent-Magnet Minimization in PM-Assisted Synchronous Reluctance Motors for Wide Speed Range," *Industry Applications, IEEE Transactions on* , vol.49, no.1, pp.31-41, Jan.-Feb. 2013.
- [5] Chino, S.; Ogasawara, S.; Miura, T.; Chiba, A.; Takemoto, M.; Hoshi, N.; "Fundamental characteristics of a ferrite permanent magnet axial gap motor with segmented rotor structure for the hybrid electric vehicle," *Energy Conversion Congress and Exposition (ECCE), 2011 IEEE* , vol., no., pp.2805-2811.
- [6] Sekerak, P.; Hrabovcova, V.; Pyrhonen, J.; Kalamen, S.; Rafajdus, P.; Onufer, M., "Comparison of Synchronous Motors With Different Permanent Magnet and Winding Types," *Magnetics, IEEE Transactions on* , vol.49, no.3, pp.1256,1263, March 2013.
- [7] Eriksson, S.; Bernhoff, H.; , "Rotor design for PM generators reflecting the unstable neodymium price," *Electrical Machines (ICEM), 2012 XXth International Conference on* , vol., no., pp.1419-1423, 2-5 Sept. 2012.
- [8] Barcaro, M.; Bianchi, N., "Interior PM Machines using Ferrite to Replace Rare-Earth Surface PM Machines," *Industry Applications, IEEE Transactions on* , vol.PP, no.99, pp.1,1, 0.
- [9] Ooi, S.; Morimoto, S.; Sanada, M.; Inoue, Y.; , "Performance evaluation of a high power density PMA SynRM with ferrite magnets," *Energy Conversion Congress and Exposition (ECCE), 2011 IEEE* , vol., no., pp.4195-4200, 17-22 Sept. 2011.
- [10] Armando, E.; Guglielmi, P.; Pastorelli, M.; Pellegrino, G.; Vagati, A., "Performance of IPM-PMASR Motors with Ferrite Injection for Home Appliance Washing Machine," *Industry Applications Society Annual Meeting, 2008. IAS '08. IEEE* , vol., no., pp.1-6.
- [11] Sanada, M.; Inoue, Y.; Morimoto, S.; "Rotor structure for reducing demagnetization of magnet in a PMA SynRM with ferrite permanent magnet and its characteristics," *Energy Conversion Congress and Exposition (ECCE), 2011 IEEE* , vol., no., pp.4189-4194.
- [12] Vagati, A.; Boazzo, B.; Guglielmi, P.; Pellegrino, G., "Design of Ferrite Assisted Synchronous Reluctance machines robust towards demagnetization," *Industry Applications, IEEE Transactions on* , vol.PP, no.99, pp.1,1, (Respective Conference Paper: Vagati, A.; Boazzo, B.; Guglielmi, P.; Pellegrino, G., "Ferrite assisted synchronous reluctance machines: A general approach," *Electrical Machines (ICEM), 2012 XXth International Conference on* , vol., no., pp.1315,1321, 2-5 Sept. 2012)
- [13] El-Refaie, A.M.; Jahns, T.M., "Comparison of synchronous PM machine types for wide constant-power speed range operation," *Industry Applications Conference, 2005. Fourtieth IAS Annual Meeting. Conference Record of the 2005* , vol.2, no., pp. 1015- 1022.
- [14] Pellegrino, G.; Vagati, A.; Guglielmi, P.; Boazzo, B.; , "Performance Comparison Between Surface-Mounted and Interior PM Motor Drives for Electric Vehicle Application," *Industrial Electronics, IEEE Transactions on* , vol.59, no.2, pp.803-811, Feb. 2012.
- [15] A. Vagati and P. Guglielmi et al., "Design, analysis and control of Interior PM synchronous machines". Tutorial Course notes of IEEE Industry Applications Society Annual Meeting (IAS), CLEUP, Padova (Italy), ISBN 88-7178-898-2, pp. 6.1-6.35, 2004.
- [16] A.Vagati, "Synchronous Reluctance Electrical Motor having a low torque ripple design", US Patent 5,818,140 – Oct.6,1998.
- [17] A. Vagati, M. Pastorelli, G. Francheschini, and S. Petrache, "Design of low-torque-ripple synchronous reluctance motors," *Industry Applications, IEEE Transactions on* , vol. 34, no. 4, pp. 758 -765, jul/aug 1998.
- [18] W. Soong and T. J. E. Miller, "Field weakening performance of brushless synchronous AC motor drives," *Proc. IEE—Elect. Power Appl.*, vol. 141, no. 6, pp. 331–340, Nov. 1994.
- [19] T. J. E. Miller Brushless PM and Reluctance Motor Drives, 1989 :Clarendon
- [20] Boazzo, B.; Pellegrino, G.; Vagati, A., "Multipolar SPM machines for direct drive application: a general design approach," *Industry Applications, IEEE Transactions on* , vol.PP, no.99, pp.1,1, 0
- [21] G. Franceschini, A. Fratta, C. Petrache, A. Vagati, and F. Villata, "Design comparison between induction and synchronous reluctance motors," in *ICEM 1994*, Paris, France, Sept. 6-8, 1994.
- [22] T. Lipo, "Introduction to AC Machine Design", University of Wisconsin Power Electronics Research Center, 1993.
- [23] Hitachi, "High Energy Ferrite Magnets – NMF Series", <http://www.hitachi-metals.co.jp/>
- [24] Armando, E.; Bojoi, R.I.; Guglielmi, P.; Pellegrino, G.; Pastorelli, M., "Experimental Identification of the Magnetic Model of Synchronous Machines," *Industry Applications, IEEE Transactions on* , vol.49, no.5, pp.2116,2125, Sept.-Oct. 2013